Acta metall. mater. Vol. 38, No. 2, pp. 143–159, 1990
Printed in Great Britain

0956-7151/90 $3.00 + 0.00
Pergamon Press plc

OVERVIEW NO. 88

ON THE INTERPRETATION OF THE FRACTAL CHARACTER OF FRACTURE SURFACES

R. H. DAUSKARDT, F. HAUBENSAK† and R. O. RITCHIE

Department of Materials Science and Mineral Engineering, University of California at Berkeley and Center for Advanced Materials, Materials and Chemical Sciences Division, Lawrence Berkeley Laboratory, 1 Cyclotron Road, Berkeley, CA 94720, U.S.A.

(*Received* 10 *November* 1988; *in revised form* 20 *June* 1989)

Abstract—To examine the usefulness of the fractal concept in quantitative fractography, a series of classical fracture surfaces, namely transgranular cleavage, intergranular fracture, microvoid coalescence, quasicleavage and intergranular microvoid coalescence, are analyzed in terms of fractal geometry. Specifically, the five brittle and ductile fracture modes are studied, from three well characterized steels (a mild steel, a low-alloy steel and a 32 wt% Mn-steel) where the salient microstructural dimensions contributing to the final fracture morphology have been measured. Resulting plots of the mean angular deviation, and Richardson (fractal) plots of the lineal roughness, as a function of the measuring step size, are interpreted with the aid of computer-simulated fracture-surface profiles with known characteristics. It is found that the ranges of resolution, over which the fractal dimension is constant, correspond to the pertinent metallurgical dimensions on the fracture surface, and thus can be related to microstructural size-scales.

Résumé—Afin d'évaluer l'utilité du concept de fractal dans la fractographie quantitative, une série de surfaces de rupture classiques—par clivage transgranulaire, rupture intergranulaire, coalescence de microcavités, pseudoclivage et coalescence de microcavités intergranulaires—sont analysées en fonction de la géométrie fractale. On étudie plus particulièrement ces cinq modes de ruptures ductiles et fragiles dans trois aciers bien connus (un acier doux, un acier faiblement allié et un acier à 32% en poids de manganèse) où l'on a mesuré les dimensions microstructurales essentielles qui contribuent à la morphologie finale de rupture. On interprète les courbes qui en résultent pour la déviation angulaire moyenne, et les courbes de Richardson (de fractal) de la rugosité linéaire à l'aide de profils de surfaces de rupture simulées par ordinateur à partir des caractéristiques connues. On trouve que les domaines de résolution pour lesquels la dimension du fractal est constante correspondent aux dimensions métallurgiques appropriées sur la surface de rupture, et peuvent donc être reliés à des échelles de taille microstructurales.

Zusammenfassung—Eine Reihe klassischer Bruchflächen, nämlich transgranulare Spaltfläche, intergranulare Bruchfläche, Zusammenwachsen von Poren, Quasispaltung und Zusammenwachsen von intergranularen Poren, werden mit Hilfe der fraktalen Geometrie analysiert, um die Nützlichkeit des fraktalen Konzeptes für die quantitative Fraktografie zu prüfen. Insbesondere werden die fünf Moden von Spröd- und Duktilbruch dreier gut charakterisierter Stähle (Flußstahl, niedrig gekohlter Stahl und Stahl mit 32 Gew.-% Mn) untersucht; in diesen Stählen waren die für die endgültige Bruchmorphologie wichtigen Maße der Mikrostruktur ermittelt worden. Diagramme der mittleren Winkelabweichung und (fraktale) Richardson-Diagramme der (eindimensional gemessenen) Rauhigkeit werden in Abhängigkeit von der Größe der Meßstufe erstellt; diese werden mit Hilfe von Computer-simulierten Profilen der Bruchoberfläche bekannter Charakteristik interpretiert. Es ergibt sich, daß die Bereiche der Auflösung, über die die fraktale Dimension konstant ist, den metallurgischen Dimensionen auf der Bruchoberfläche entsprechen und daher mit den Größenmaßstäben der Mikrostruktur verknüpft werden können.

1. INTRODUCTION

The application of fractal geometry provides an effective tool in the study of highly irregular surfaces. Here, the concept of a "fractal dimension" is employed to characterize the space-filling ability of a continuous, non-differentiable curve [1]. Many of these so-called *fractal curves* have the important invariance property of self-similarity under scale transformations. Indeed, the repetition of essentially the same features, as the curve is viewed under increasing magnification, is a sufficient condition to guarantee the existence of a well defined fractal dimension. Naturally, in practice the magnification is restricted to a particular range of interest or

†Present address: Department of Materials Science and Engineering, Massachusetts Institute of Technology, Cambridge, MA 02139, U.S.A.

experimental feasibility, and the fractal dimension confined to that range.

Although the true fractal nature of naturally occurring systems may be disputed, experimental evidence suggests that self-similarity and fractal character may be exhibited over significant ranges of interest. Indeed, the remarkable progress that has occurred in understanding the structure of a variety of naturally occurring forms and growth processes using fractal geometry is exemplified by a collection of papers edited by Stanely and Ostrowsky [2]. Additional studies employing monolayer adsorption techniques for a range of chemical surface adsorbents have revealed the fractal character of selected surfaces from atomic to molecular dimensions [3–5]. These surfaces impose on the adsorbate atoms or molecules intermolecular conditions intermediate between those of a two-dimensional and three-dimensional structure. Investigations of several proteins using independent electron spin relaxation and X-ray measurements have similarly revealed the fractal form of the protein backbone and its resemblance to the self-avoiding random walk with a fractal dimension of 5/3, intermediate between that of a one-dimensional line and two-dimensional surface [6]. Research has also revealed the self-similar character and fractal nature of sandstone porosity [7] and fine particle profiles [8, 9]; in fact, fractal techniques have been used to facilitate the research of cartographic lines in urban development studies [10].

Fractal geometry has found particular application in the characterization of fracture surfaces [2, 11–14], where the fractal dimension has been used as a quantitative indicator of the roughness of a fracture surface or its profile. Indeed, an inherent propensity of microstructural features to fractal analysis has been suggested [1, 2, 11, 16, 17], and fractography has been highlighted as a principal application of fractal geometry in several recent reviews [18–20]. However, although much data have been generated to quantify particular fracture surfaces, an understanding of the true relevance and limitations of the fractal concept on well characterized fracture modes is still lacking.

1.1. The fractal dimension

1.1.1. Definition. Precise definition of the fractal dimension is almost as elusive as the curious properties of fractal geometry itself. From a rigorous mathematical perspective, a set of points is said to exhibit fractal behavior when the *Hausdorff (or "fractal") dimension is strictly non-integer*, having fractional values between those of the intuitive topological dimensions of 0, 1, 2, etc. [1]. With a view to developing a test for the fractal character of naturally occurring systems, a prominent property is the scale-dependent behavior of many observed physical properties. A classic example is Richardson's measurements of the length of continental coastlines [1], where the length measured depends on the measuring scale; the finer the scale, the longer the length. An important additional phenomenon is that of *self-similarity*; although not all fractals are self-similar, self-similarity does provide a necessary and sufficient condition for the Hausdorff dimension to be uniquely defined. Naturally occurring fractals may lack the regularity of geometrically constructed one; nevertheless, they are most often self-similar in a statistical sense.

To provide an operational definition for the fractal behavior of a set of points, Richardson's structured walk method [1] can be used; this approach is analogous to walking a pair of dividers with fixed span along a boundary and counting the number of steps. The empirical relationship postulated by Richardson between the profile length, L, and the measuring step size, η, is

$$L = L_0 \eta^{(1-D)} \tag{1}$$

where L_0 is a constant and the value of the non-integer exponent D, which is independent of η, is dependent on the particular boundary being studied; Mandelbrot [1] subsequently showed that D may be interpreted as the fractal dimension of the curve or boundary. For geometrically constructed fractal curves, where the length of the profile is unbounded, the fractal dimension succinctly describes the behavior of the profile length with measuring scale; moreover, the value of D appears to be characteristic of the degree of roughness of the curve [8, 14]. In physical systems, however, fractal behavior is confined within limiting dimensions, such as between the size of an atom or molecule and the macroscopic size of the system being investigated.

1.1.2. Application to fractography. Experimental methods used to obtain fractal information from fracture surfaces involve either obtaining fracture-surface profiles from metallographic sections cut perpendicular to the fracture plane ("vertical section method"), or from sequentially prepared sections parallel to the fracture plane ("slit island technique") [11, 14]. In the present study, the vertical section method was used, and analyzed in terms of the structured walk technique [equation (1)]. Accordingly, equation (1) is normalized by the projected length of the profile, L', to obtain an expression for the lineal roughness parameter, R_L

$$R_L = L/L' = R_o \eta^{(1-D)} \tag{2}$$

where R_0 is a constant. Dimensions over which fractal character is exhibited by the profiles can then be obtained from the extent of linearity of (Richardson) plots of $\log(R_L)$ vs $\log(\eta)$.

Surfaces were also characterized by the angular distribution of the linear segments (measuring steps) along the fracture profile to provide a local measure of the angle of deflection of the crack path. This was described in terms of the mean angular deviation, $\bar{\theta}$, defined as the average deviation of the segment normals from a pre-defined reference direction.

1.2. Characteristic fracture dimensions

Fracture-surface morphologies represent a complex mosaic of microstructural artifacts, the features of which are characteristic of the particular fracture mode and microstructure and may range in size from the atomic dimensions of dislocation slip steps to the macroscopic dimensions of grain size. Understanding of this morphology requires the deconvolution of these characteristic dimensions which together form the "building blocks" of the fracture surface. Characteristic fracture dimensions are related to significant microstructural lengths which influence the specific *local* micromechanisms of fracture.

Fracture processes may be categorized into three principal morphologies, namely, microvoid coalescence, intergranular fracture and transgranular cleavage. (Several less common processes have also been documented, including quasicleavage and intergranular microvoid coalescence.) Each of these processes reflects a substantially different local failure criterion and dependence on microstructure, and displays a definitive morphology with distinct characteristic dimensions. In view of the specificity of models to describe a particular fracture mechanism, however, complete characterizations have only been achieved in a few simplified cases (as reviewed in Ref. [21]); the principal mechanisms are summarized below.

For transgranular cleavage, the onset of brittle crack extension has been modelled in terms of the local principal stress ahead of the crack exceeding a local fracture stress *over a microstructurally significant distance* [22]. In statistical terms, this characteristic dimension represents the location from the crack tip of the most probable initial fracture event and reflects the mutual competition of high stresses *close* to the tip and an increasing probability of finding a "weak link" (e.g. large brittle particle) to initiate fracture *away* from the tip [23]. In mild steels, it is of the order of the spacing of the grain-boundary carbides, i.e. typically a few ferrite grain diameters [22]. Models for brittle intergranular fracture can be similarly constructed [24, 25]. Alternatively, ductile fracture by microvoid coalescence can be modelled in terms of a (stress modified) critical strain criterion [26–28]: here the local equivalent strain ahead of the tip must exceed a critical fracture strain (specific to the prevailing stress state) over a characteristic (radial) distance from the tip, which is now comparable with the spacing of the main void-initiating particles. In this manner, microstructural features over a wide range of dimensions can influence specific fracture morphologies in distinct ways.

Variation in characteristic dimensions with fracture mode, which in turn is influenced by such variables as stress state, test temperature, and material system, has generally confused attempts to correlate the fracture energy with the fractal dimension D [11, 14, 15, 29]. For cleavage fracture in metals, correlations between, for example, the Griffith fracture energy and D may be plausible, albeit tenuous, yet in the majority of fractures where plastic work is involved, they have little specious physical basis. Conversely, correlations [13] between the fatigue crack growth threshold and D may be quite appropriate, since at near-threshold levels, near-tip stress intensities are often strongly influenced by crack deflection and resulting crack closure induced by the wedging action of crack-surface asperities [30], both crack-tip shielding mechanisms which are highly dependent on the fracture-surface roughness.

In the present work, a simple numerical model is constructed to simulate fractal profiles using well defined distributions of segments representing the fracture-surface roughness at both microscopic and macroscopic levels. Ranges of dimension over which fractal character is exhibited are then observed and correlated to parameters describing the segment distributions. The results of this study are used to interpret the fractal character of the principal fracture modes in terms of the salient dimensions associated with the fracture surface and underlying microstructure.

2. PROCEDURES

2.1. Numerical simulations

Fracture-surface profiles were simulated using defined distributions of segments, representative of significant microstructural dimensions. The model incorporates known distributions of interconnected segment lengths, chosen to depict both the macroscopic and microscopic roughness of the fracture surface (Fig. 1). In its simplest form [Fig. 1(a)], macro-roughness is simulated using a single Gaussian distribution of segment lengths with known mean and standard deviation. Appropriate computer code is utilized to generate a digitized profile by selecting segment lengths from a pseudo-random number generator, and connecting them end to end in a zig-zag fashion at fixed angles $\pm\theta$ from the horizontal. In this way, the effect of varying mean segment length M (units), standard deviation S (units), and mean angular deviation $\bar{\theta}$, on the fractal dimension could be assessed independently.

The effect of the micro-roughness of the fracture surfaces was evaluated by superimposing a second Gaussian distribution of segment lengths with smaller mean, m (units), and standard deviation, s (units); these segments were connected in zig-zag fashion at fixed angles $\pm\phi$ from a line connecting the end points of the macro-roughness segment [Fig. 1(b)].

The simulated profiles were analyzed in identical fashion to that used for the actual fracture-surface profiles. Specifically, mean angular deviation, $\bar{\theta}$, and linear roughness parameters, R_L, were computed and plotted as a function of the measuring step size, η; linear regions on the R_L/η plots indicate fractal behavior over the range in question.

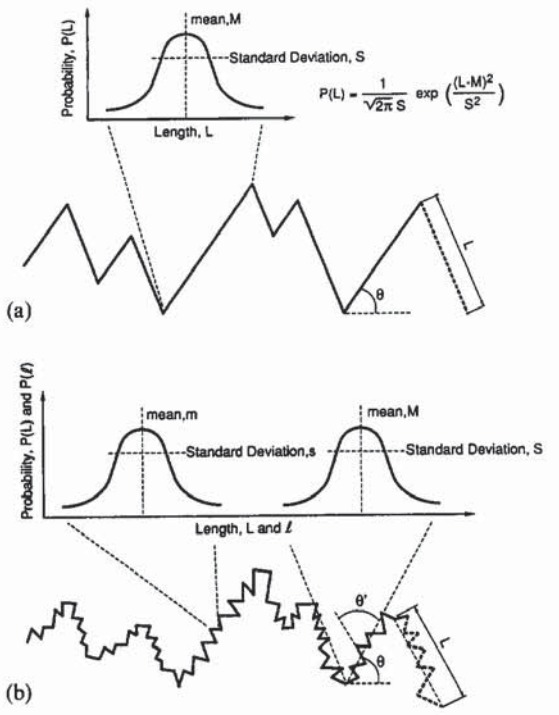

Fig. 1. Schematic illustration of model used to simulate fracture profiles using known Gaussian distributions of segment lengths with mean segment length, M, standard deviation, S, and mean angular deviation, $\bar{\theta}$. The model incorporates (a) a single distribution of segment lengths representing the effects of macro-roughness, and (b) a second distribution of smaller segment lengths superimposed on the larger segments representing both micro- and macro-roughness.

2.2. Experimental procedures

2.2.1. Materials. Fracture surfaces, representing the "classical" fracture modes of transgranular cleavage, brittle intergranular fracture, microvoid coalescence, intergranular microvoid coalescence and quasicleavage, were obtained by fracturing Charpy V-notch specimens of an AISI 1008 mild steel, a 31 wt% Mn-steel, and a low alloy ASTM A533B Class 2 nuclear pressure-vessel steel (in as-received, hydrogen charged and hydrogen attacked conditions) at ambient and liquid-nitrogen temperatures. Alloy compositions are listed in Table 1.

2.2.2. Microstructures. The mild steel had a ferritic microstructure with regions of pearlite at grain boundaries (ferrite grain size $\sim$10 to 75 μm, mean $\sim$28 μm). The manganese steel consisted of fully austenitic equiaxed grains, with evidence of manganese-sulfide/manganese-oxide inclusions (grain size $\sim$20 to 150 μm, mean $\sim$56 μm; particle spacing $\sim$6 to 15 μm, mean $\sim$10 μm) [31]. The A533B steel, conversely, showed a banded, tempered martensitic structure with cementite particles at prior austenite grain boundaries (prior austenite grain size $\sim$50 to 200 μm, mean $\sim$100 μm) [32]. Although no microstructural differences were obvious after hydrogen charging the A533B steel in HCl solution, the hydrogen attacked condition in A533B (following exposure to high pressure ($\sim$16 MPa) hydrogen gas for 1400 h at $\sim$550°C) showed evidence of decarburization and arrays of micron-sized microvoids (from the formation of methane bubbles) decorating prior austenite grain boundaries. Clusters of microvoids formed preferentially on boundaries parallel to the rolling plane; this created "fissures" with a size and spacing of $\sim$250 to 440 μm, and mean of 300 μm [32, 33].

2.2.3. Metallography. Fracture surfaces were electrolytically plated with nickel, and sectioned normal to their plane; the resulting fracture profiles were mounted, optically polished and lightly etched in 2% nital. Two representative optical micrographs were taken at magnifications of 20, 200, and 2000 $\times$, and digitized using a digitizing table. At each magnification, points along the profile boundary about one millimeter apart were taken as the limit of resolution; the selected magnification ranges therefore resulted in sufficient overlap so that features at the resolution limit of one magnification could be easily resolved at the higher magnification.

2.3. Data analysis

To facilitate investigation of the scale dependence of the lineal roughness and mean angular deviation, the measuring step length was varied by logarithmically increasing the number of digitized points within the measured segment. Digitized profile data at the three magnifications were used to generate independent sets of profile parameter data; these were subsequently combined to form one set describing the fracture surface over a wide range of resolution from 0.5 μm to 2 mm. This method of data acquisition requires far fewer optical micrographs than that required for a montage of higher magnification micrographs.

Typical sets of experimental lineal roughness vs. step size data at the three magnifications is shown in Fig. 2 (from an intergranular morphology in the Mn-steel). The two curves obtained at higher magnifications are shifted to higher R_L values to simulate the effect of obtaining the entire curve at one magnification; the magnitude of the shift is estimated in the following manner. Considering curves 2 and 3 in

Table 1. Composition of alloys investigated in wt%

Alloy	Fe	Cr	Ni	Mo	Mn	Si	N	S	P	O	C
AISI 1008	bal	—	—	—	0.26	0.01	—	0.01	0.010	—	0.080
31Mn-steel	bal	—	—	—	31.0	—	0.03	0.01	<0.005	0.02	0.006
ASTM A533B	bal	0.07	0.63	0.4	1.29	0.16	—	0.01	0.010	—	0.250

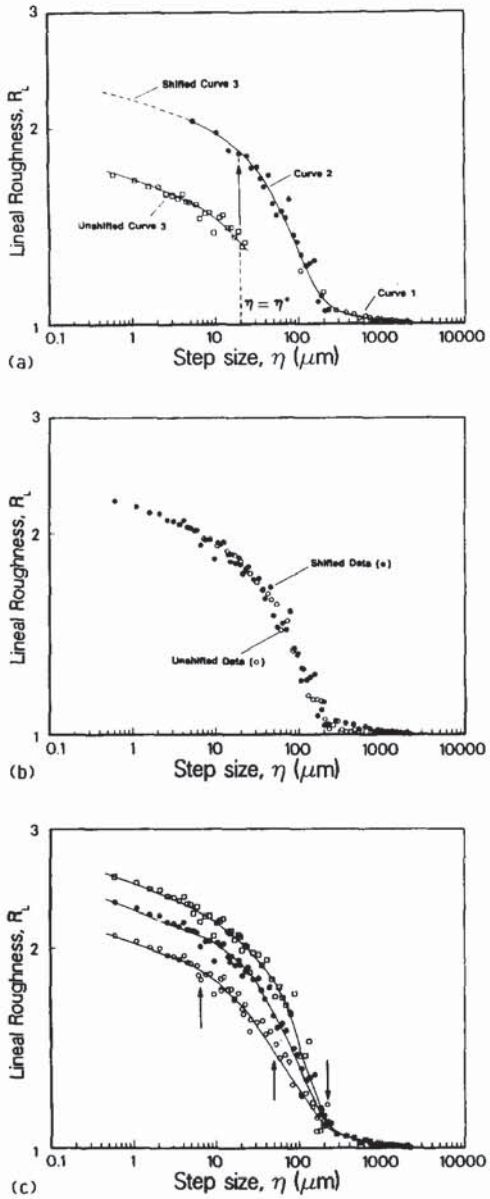

Fig. 2. Illustration of the variation in lineal roughness parameter. R_L, with measuring step size, η, obtained at the three magnifications, showing (a) shifting algorithm which requires $R_{L2} = = R_{L3}$ when $\eta = \eta^*$, (b) match of shifted data with results obtained from montage of 24 micrographs at 1000 ×, and (c) uncertainty in fractal dimension. [Vertical arrows in (c) represent the limiting dimensions governing the validity of a particular fractal.]

Fig. 2(a). it is required that $R_{L2} = R_{L3}$ when $\eta = \eta^*$. Using

$$R_{L2} = \frac{\sum_1^k \eta}{L_{o2}} \tag{3}$$

and

$$R_{L3} = \frac{\sum_1^n \eta}{L_{o3}} \tag{4}$$

where L_{o2} and k, and L_{o3} and n are the projected lengths of, and number of measuring step lengths counted for, curves 2 and 3, respectively. We require that

$$\frac{\sum_1^k \eta}{L_{o2}} = \frac{\sum_1^n \eta}{L_{o3}} \tag{5}$$

from which the new projected length of curve 2, L'_{o3}, can be obtained

$$L'_{o3} = (n/k) L_{o2}. \tag{6}$$

This approach was validated by comparing the modified set of data in Fig. 2(a) to a control set, obtained by analyzing a montage of 25 micrographs at 1000 × magnification; results showed that the two plots matched closely [Fig. 2(b)].

The uncertainty in measured fractal dimensions were evaluated by estimating the scatter associated with these data by sampling the profiles in a random fashion without disregarding anomalous features [Fig. 2(c)]. Based on these results, the uncertainty in maximum fractal dimensions was found to be of the order of ±7%; however, the characteristic dimensions governing their range of validity were largely unaffected.

3. RESULTS

3.1. Characterization of numerically simulated fracture-surface profiles

Log–log plots of linear roughness R_L vs measuring step size η for the computer generated profiles are presented in Figs 3–7; inserts show the simulated profile morphologies, and the Gaussian distributions of segment lengths used to generate each profile are indicated on the abscissa.

The R_L/η plots from profiles generated by the single distribution of segments, which simulate varying degrees of macro-roughness (Figs 3 and 4), show the sigmoidal shape commonly observed for material fracture profiles [12, 14]. The center linear section represents a range of dimension over which the profile closely approximates a true fractal curve; deviations from linearity at either end can result from a loss of resolution in the measuring technique, but ideally indicate where the profile no longer approximates a fractal curve.

The $\bar{\theta}/\eta$ plots of mean angular deviation of the measuring steps along the profile exhibited trends essentially similar to that observed for the R_L parameter. In particular, marked increases in $\bar{\theta}$, indicative of increased local roughness on a scale of the measuring step size, were apparent with decreasing measuring step size over ranges corresponding to fractal (linear) behavior in the R_L/η plots.

3.1.1. Effect of mean segment length. The effect of varying macro-roughness in terms of the mean segment length, M, is shown in Fig. 3; the standard

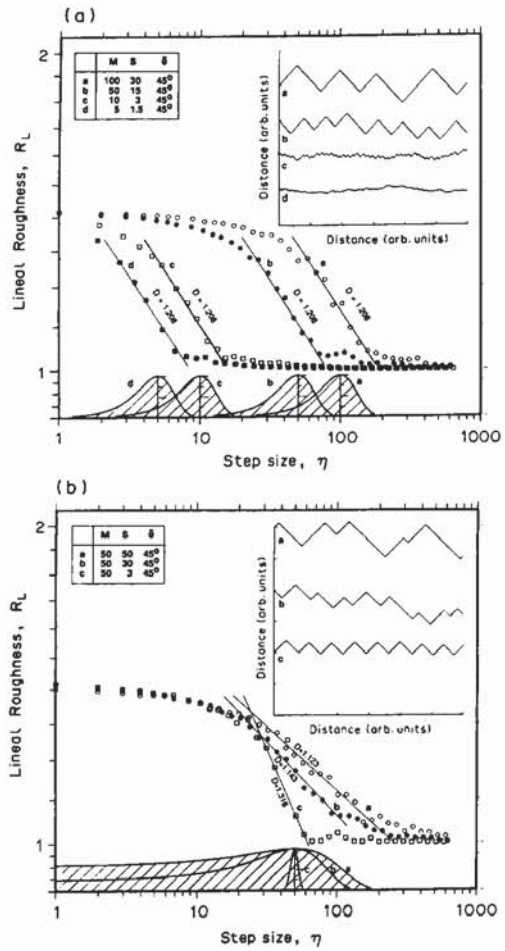

Fig. 3. The effect of (a) varying mean segment length, M, and (b) varying standard deviation, S, on the relationship between linear roughness, R_L, and the measuring step size, η, for numerically simulated profiles generated using single distributions of segment lengths. Representative sections of the profiles, together with the segment distributions and fractal dimensions of the linear sections of the curves are included for comparison.

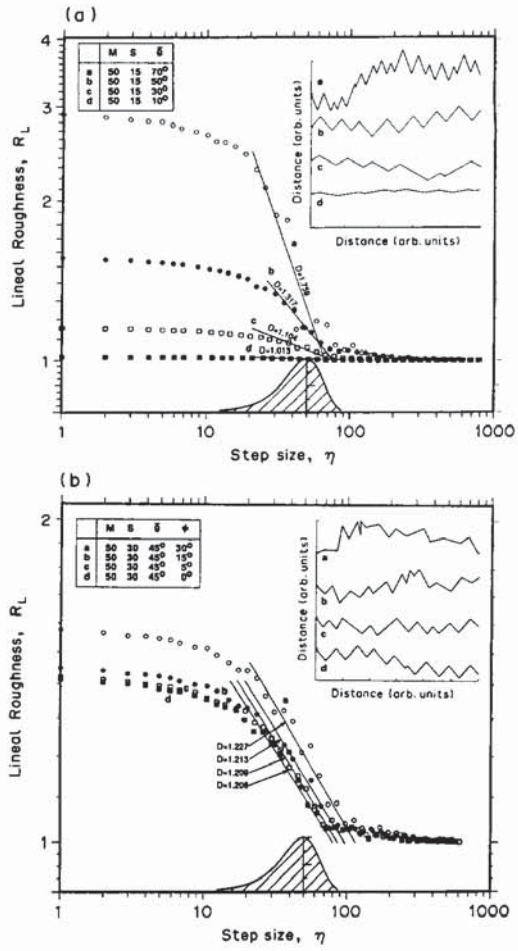

Fig. 4. The effect of varying (a) mean angular deviation, $\bar{\theta}$, from 10° to 70° with $\phi = 0°$ and (b) the standard deviation $\phi = 0°$ to 30° with $\bar{\theta} = 45°$, on the relationship between linear roughness, R_L, and the measuring step size, η, for numerically simulated profiles generated using single distributions of segment lengths.

deviation, S, of the segment distribution is held constant at 30% of the mean. As expected, the fractal dimension D of the linear sections is independent of the position of the mean, with a constant value of 1.208; points of first deviation from linearity are summarized in Table 2. It is apparent that fractal character is exhibited from about $1.5\,S$ above the mean to roughly $0.5\,M$ below the mean. Although not mathematically rigorous, this information assists in the interpretation of more complex profiles exhibiting multiple linear sections in their profile curves. It should be noted that the mean of the segment distribution is contained *within* the linear (fractal) portion of the profile curve and not at one of the inflection points, as has been previously implied [9, 11].

3.1.2. Effect of standard deviation of the mean. The effect of varying the standard deviation, S, of the segment distribution on the fractal character of the profiles is indicated in Fig. 3(b); the segment-distribution mean was held constant at 50. From the slope of the linear sections and the constant R_0 [in equation (2)] display an inverse relationship with S; D increases from 1.123 ($S = 100\%\ M$) to 1.316 ($S = 6\%$ M). The range of dimension over which fractal character is exhibited is consistent with Table 2; the upper point of first deviation from linearity is dependent on S and occurs at $\sim 1.6\,S$ above the mean, the lower deviation point, however, is insensitive to S and occurs at $\sim 0.58\,M$ below the mean.

3.1.3. Effect of angular deviation. The corresponding effect of the angular deviation of segments on the resulting profile and R_L/η curves is presented in Fig. 4 for the simplest case of a single valued mean angular deviation, $\bar{\theta}$, or for the most generalized form of a normal distribution of angular deviations with mean, $\bar{\theta}$, and standard deviation, ϕ. The fractal dimension is highly sensitive to mean angular deviation [Fig. 4(a)]; D increases from 1.013 ($\bar{\theta} = 10°$) to 1.759 ($\bar{\theta} = 70°$). (Note here the sensitive nature of the

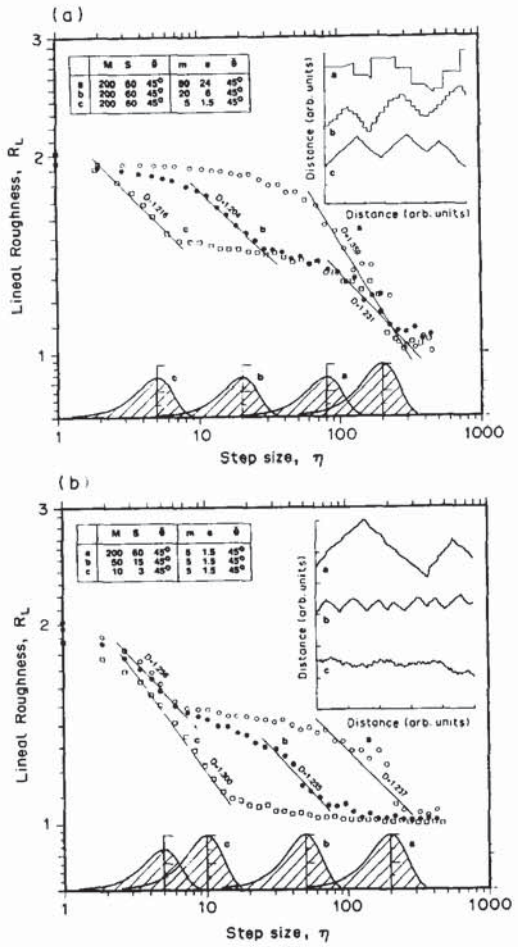

Fig. 5. The effect of (a) varying micro-roughness superimposed on a fixed macro-roughness, and (b) varying macro-roughness with a fixed micro-roughness, on the relationship between linear roughness, R_L, and the measuring step size, η. The numerically simulated profiles are generated using selected distributions of smaller segment lengths, with mean, m, and standrd deviation, s, on a fixed distribution of larger segment lengths with mean, M, and standard deviation, S.

fractal dimension as an indicator of roughness of the profile, as D varies from that of a one-dimensional line at low $\bar{\theta}$ to that approaching a two-dimensional plane at high $\bar{\theta}$.) Conversely, the distribution of angular deviations has only a marginal influence on the R_L/η plots [Fig. 4(b)]; for profiles with angular distributions with a mean of 45°, appreciable changes in D are only apparent for standard deviations in excess of 15°.

3.1.4. Effect of micro- and macro-roughness. To simulate the role of both micro- and macroroughness, the influence of two segment distributions was examined on the resulting fractal behavior of profiles. The effect of selected small scale segment distributions (means, m, and standard deviation, s), superimposed on a large scale segment distribution (mean, M, and standard deviation, S), is presented in Fig. 5. In general, the lineal roughness remains relatively insensitive to the degree of micro-roughness until the measuring step size approaches the dimension of this micro-roughness, wherein R_L shows a marked increase with decreasing η.

Where the means of the small and large scale segment distributions are sufficiently separated to minimize interaction effects, two separate linear sections in the R_L/η plot are apparent; these sections represent ranges of dimension corresponding to the two segment distributions over which the profiles display fractal character. Both the extent and slope of the linear sections exhibit the same dependence on the segment-distribution mean and standard distribution as observed for the single segment-distribution profiles.

3.1.5. Effects of overlaying segment distributions. The effect of increasing the overlap of the small and large scale segment distributions is shown in Fig. 6; this results in increasing R_L and D values, but less defined linear sections in the R_L/η curves.

3.1.6. Effect of mean angular deviation of micro-roughness. The effect of increasing mean angular deviation of the small scale segment distribution is shown in Fig. 7; this results in an increase in R_L values, markedly in the small scale, and marginally in the large scale, segment-distribution ranges of dimension.

3.1.7. Anomalous behavior of profiles with single segment length. Somewhat different R_L/η behavior is shown in Fig. 8 for profiles generated with a single segment length (standard deviation = 0) of 50 units. The pronounced sigmoidal shape of the curve precludes accurate specification of any linear regions; however, of note are the peaks in R_L which occur when η approaches the segment length of 50, and at multiples of 50 above, and at factors of 50 below. Similar behavior is apparent in other simulated profiles [notable Fig. 3(b)], and has been observed in R_L/η plots characterizing fracture surfaces in a titanium alloy [14]. Although clearly not fractal in nature, such peaks may provide a measure of the mean and distribution of segment lengths in the evaluation of an unknown surface.

3.2. Characterization of fracture-surface profiles

The five distinct fracture morphologies and their respective microstructural and fractographic dimensions are listed in Table 3; also shown are the measured fractal dimensions from R_L/η plots and the range of dimension over which such fractal behavior is manifest. Each fracture morphology is now discussed in turn.

3.2.1. Transgranular cleavage. Brittle transgranular cleavage fracture was induced by fracturing mild steel at −196°C. The resulting fractography, in the form of an optical micrograph of the fracture profile and scanning electron micrographs of the fracture surface, are illustrated in Fig. 9; also shown are the corresponding plots of lineal roughness, R_L, and mean angular deviation, $\bar{\theta}$, as a function of step size, η.

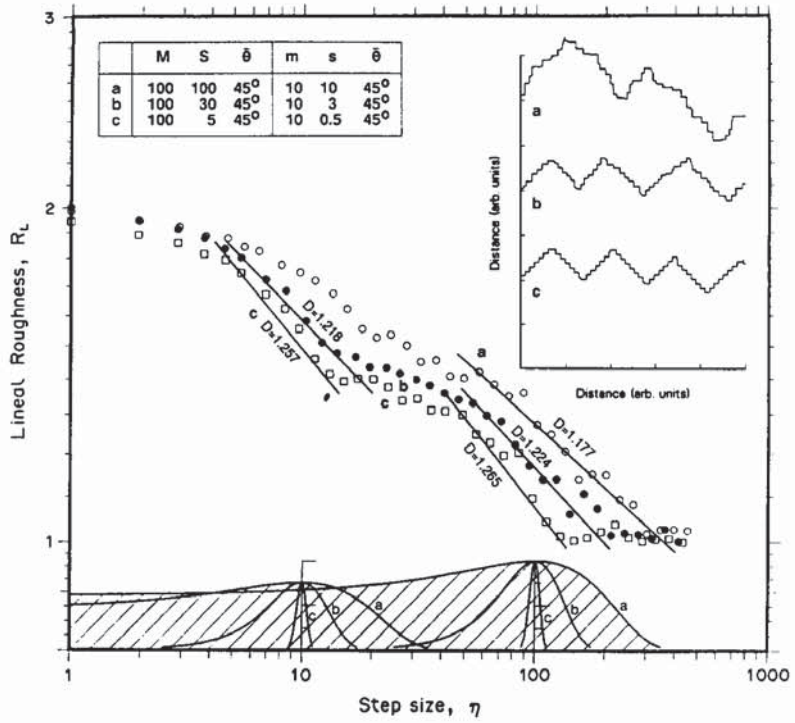

Fig. 6. The effect of increasing overlay of macro- and micro-roughness distributions on the relationship between linear roughness, R_L, and the measuring step size, η, for numerically simulated profiles.

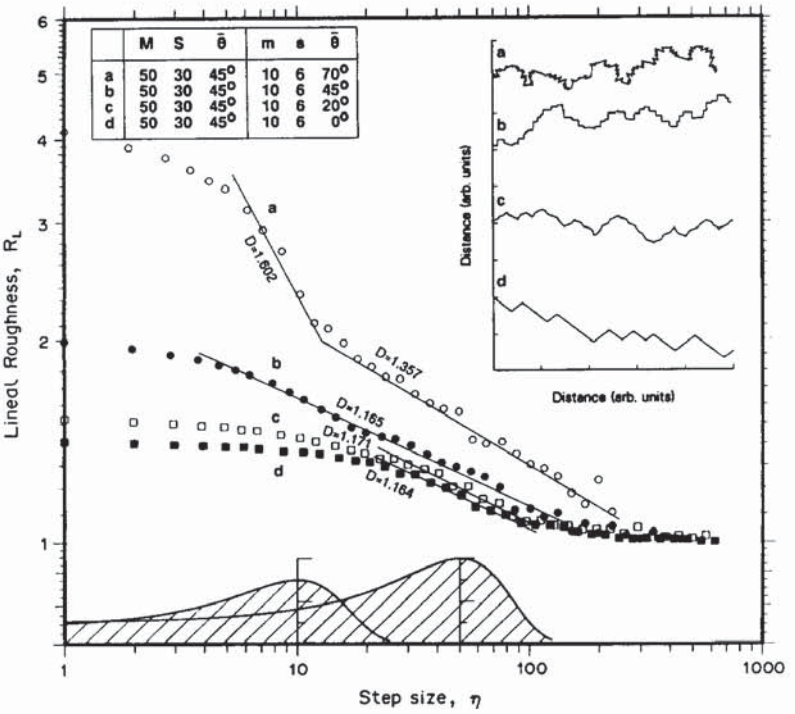

Fig. 7. The effect of increasing mean angular deviation of micro-roughness with a fixed macro-roughness on the relationship between linear roughness, R_L, and the measuring step size, η, for numerically simulated profiles.

Table 2. Limits of linear (fractal) section of R_L/η curves wtih varying mean segment length

Mean segment length	M	100	50	10	5
Standard deviation	S	30	15	3	1.5
Lower limit	$(\%M)$	55 (55)	25 (50)	5.3 (53)	2.6 (52)
Upper limit $M + as$	(a)	148 (1.6)	74 (1.6)	14.5 (1.5)	7.2 (1.4)

From Fig. 9, it is apparent that the dominant fractographic feature is the cleavage facet size, which is equivalent to the ferrite grain size of ~10 to 75 μm; this results in a fractal dimension of 1.08 over step-sizes from ~15 to 75 μm. Below ~15 μm, however, the fractal dimension changes to 1.02 over a range of step-sizes corresponding to the size of the cleavage steps and "river patterns" on these facets (~2 to 15 μm); this new fractal behavior prevails to step-sizes below a micron. Similar trends, albeit not as distinctive, are evident when the profile is characterized in terms of the mean angular deviation.

For a single fracture mode, therefore, more than one fractal dimension can exist, the range of validity of such fractals can be associated with prominent fractographic/microstructural features, and with decreasing roughness (i.e. from the cleavage facet to cleavage step size), the value of the fractal dimension is decreased.

3.2.2. Microvoid coalescence. A ductile microvoid coalescence fracture mode was obtained by impact fracture of the *Mn*-steel at room temperature; resulting fractography and corresponding R_L/η and $\bar{\theta}/\eta$ plots are shown in Fig. 10. Two conspicuous fractographic features are evident: (i) the dimples, the size and spacing of which is related to the inclusion spacing (~6 to 50 μm), and (ii) the ripples, or slip steps (~0.8 to 4 μm) on the dimple walls. Accordingly, the fracture surface again cannot be characterized by a single fractal dimension; rather two fractal dimensions, of 1.18 for the dimples and 1.06 for the (less rough) slip steps, can be defined from the R_L/η plot, and are found to be constant over the appropriate fractographic dimensions (Table 3). Trends for the $\bar{\theta}/\eta$ data, exhibiting two regions of behavior, were apparent over similar ranges of dimension.

3.2.3. Intergranular fracture. A brittle intergranular cracking mode was obtained by fracturing the Mn-steel at −196°C; fractography and R_L/η and $\bar{\theta}/\eta$ plots are shown in Fig. 11. Three almost linear regions are now apparent on the R_L/η plot; each region again corresponds to a specific fractal dimension existing over a size-scale range associated with a prominent fractographic feature. The most conspicuous feature is the grain-boundary facets, whose size is a direct function of the austenitic grain size (~20 to 150 μm);

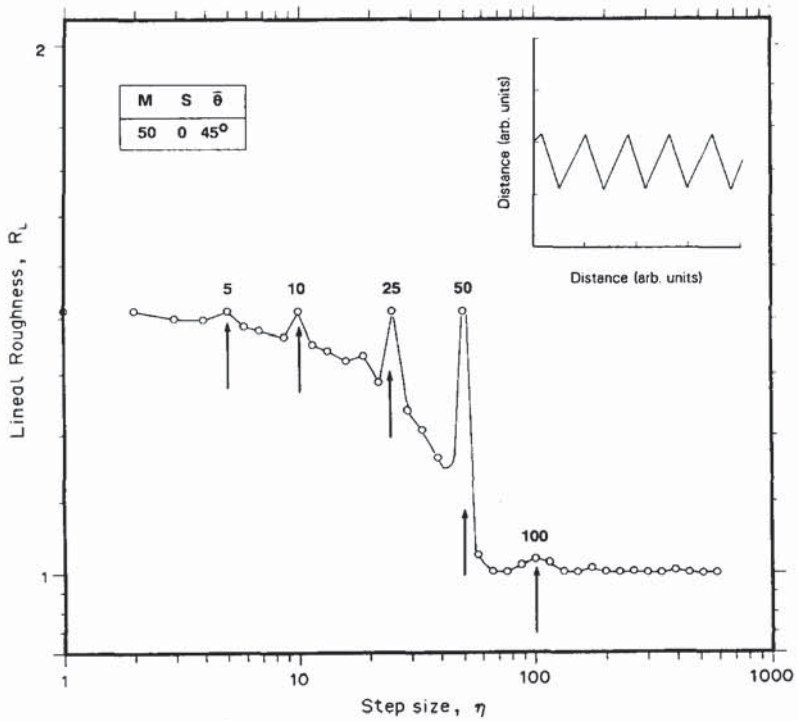

Fig. 8. Anomalous R_L/η behavior for numerically simulated profiles generated with a single segment length (of 50 units, with a standard deviation of $\bar{\theta}$), showing pronounced sigmoidal curve shape with peaks where η approaches the segment length of 50, and at multiples of 50 above, and factors of 50 below, this length.

Table 3. Comparison of fractal dimensions and validity ranges on R_L/η plots with characteristic microstructural and fractographic dimensions

Fracture mode	Structural feature	Size range and (mean) (μm)	Range of fractal behavior (μm)	Fractal dimension D
AISI 1008 steel				
Transgranular cleavage	α grain size	10–75 (28)	15–75	1.08
	cleavage steps	2–15 (15)	1–15	1.02
31 wt% Mn-steel				
Microvoid coalescence	particle spacing	6–50 (20)	5–150	1.18
	slip steps	0.8–4 (1)	0.6–5	1.06
Intergranular fracture	γ grain size	20–150 (56)	35–200	1.26
	[a]gb particle spacing	6–15 (10)	6–20	1.09
	[a]gb slip steps	0.8–4 (1)	0.6–5	1.06
A533B Steel				
Quasicleavage	γ grain size	50–200 (100)	80–1000	1.01
(−196°C)	"flag segments"	1–31	0.6–80	1.08
(*H* charged)	γ grain size	50–200	80–1000	1.06
	"flat segments"	2–70	0.6–80	1.12
Ductile intergranular	banded structure and fissures	250–440 (300)	200–1000	1.04
(*H* attacked)	grain size	5–100 (19)	10–200	1.14
	CH_4 bubble size	0.4–3 (1)	0.6–9	1.08

[a]gb refers to grain boundary.

these result in a constant fractal dimension of 1.28 over the range ~35 to 200 μm. However, fractographic features on the grain-boundary surfaces, specifically particles (spacing ~6 to 15 μm) and slip-steps (spacing ~0.8 to 4 μm), result in additional fractal dimensions of 1.09 and 1.06, respectively; each fractal is again valid over a range of step sizes comparable with the specific fractographic dimensions. Corresponding plots of the mean angular deviation, as a function of η, for this fracture surface show similar prominent dimension ranges of ~40 to 250 μm, ~4 to 12 μm and ~0.6 to 4 μm, which appear to correlate to ranges of fractal behavior.

3.2.4. Quasicleavage. Figures 12 and 13 both show quasicleavage fracture induced by the impact failure of A533B steel at −196°C in the uncharged and hydrogen charged conditions, respectively. Both fracture surfaces display the "feathery" facets characteristic of quasicleavage, with dimensions comparable to the prior austenite grain size (~50 to 200 μm); this is reflected on R_L/η plots as a fractal dimension of 1.01 to 1.06 between ~80 and 1000 μm. The surfaces also display fractographic features at smaller size scales, in the form of characteristic ridges and steps on quasicleavage facets, which appear as "flat segments" of the order of 1 to 70 μm in size. These segments represent where the crack path experienced small changes in direction due to encounters with martensite-packet boundaries, and additionally in the case of the hydrogen charged microstructure, locally embrittled lath boundaries [34]. A second fractal dimension thus is apparent at smaller values on the R_L/η plot, with a range of validity (~0.6 to 5 μm) comparable with the size range of the segments.

Of note is that the two examples of quasicleavage result from the same steel microstructure, but hydrogen embrittlement in the charged structure induces a similar, yet rougher and more tortuous, fracture surface. The two surfaces thus have similar R_L/η and $\bar{\theta}/\eta$ plots indicative of their similar morphologies, but with a larger fractal dimension for the hydrogen charged specimen.

3.2.5. Ductile intergranular fracture. By prior exposure of the A533B steel to high-temperature/high-pressure hydrogen, severe microstructural damage from hydrogen attack can be induced in the form of grain-boundary distributions of microvoids and larger fissures (from methane-bubble formation) [32, 33]; this results at −196°C in an intergranular microvoid coalescence mechanism, reminiscent of creep cavitation fracture [35], along prior austenite grain boundaries (Fig. 14). With this mechanism, three regions with constant fractal dimension are evident, which again can be related to characteristic microstructural dimensions.

At the largest size scales, the fracture morphology is dominated by the presence of fissures, generated by the preferential formation, and coalescence, of methane bubbles at locations of high cementite concentration in the banded microstructure. These features have a typical size and spacing of ~250 to 400 μm with $D = 1.04$ over ~200 to 1000 μm. Between 10 and 200 μm, $D = 1.14$, reflecting the morphology of the intergranular facet size, which in turn is a function of the prior austenite grain size (~5 and 100 μm). Finally, between ~0.6 and 9 μm, a third fractal dimension ($D = 1.08$) is evident, consistent with size of the microvoid dimples (from methane bubbles) on the grain-boundary facets (Table 3).

4. DISCUSSION

The precise relevance of the fractal dimension as a measure of fracture-surface roughness and its application to defining fracture-toughness and crack-growth behavior remains uncertain unless an

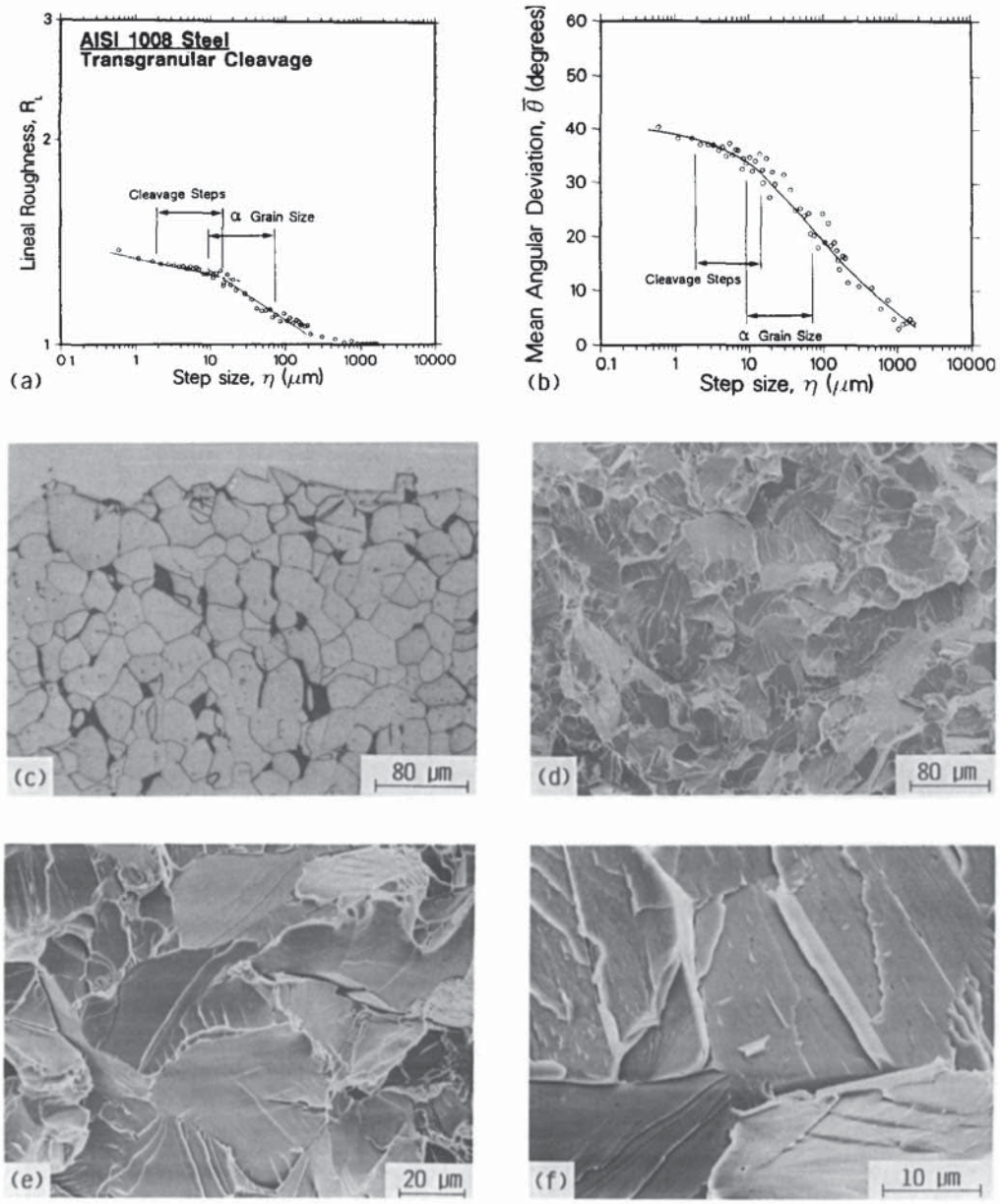

Fig. 9. Fractal characteristics of transgranular cleavage fracture, of mild steel at −196°C, showing plots of (a) lineal roughness, R_L, and (b) mean angular deviation, $\bar{\theta}$, as a function of measuring step size, η, (c) optical micrograph of crack-surface profile, and (d–f) scanning electron micrographs of fracture surface at increasing magnifications.

understanding of the microstructural origins and range of the fractal behavior can be afforded. The present study focuses attention on the fractal behavior, within a bounded range of dimension, of a distribution of characteristic fracture dimensions which form the building blocks of fracture profiles. Systems involving *single* characteristic dimensions, such as particle size to simulate agglomerates, have been examined and exhibit two fractal relationships at dimensions above and below that of the particle size, where the terms "structural" and "textural" fractal have been suggested to describe the two regimes, respectively [9]. Prior to the present work, however, the effect of a *distribution* of characteristic fracture dimensions (particle spacings, grain sizes, etc.) had not been specifically addressed. Although simulation of mathematically rigorous fractal fracture profiles is impossible (since an unbounded range of elements of decreasing size is not available), so-called structural and textural fractal behavior may still be expected.

Indeed, computer simulated fracture profiles using Gaussian distributions of segment lengths clearly establish that fractal character is exhibited over a range of size scales that is included in the distribution of segment lengths. The range of fractal behavior can

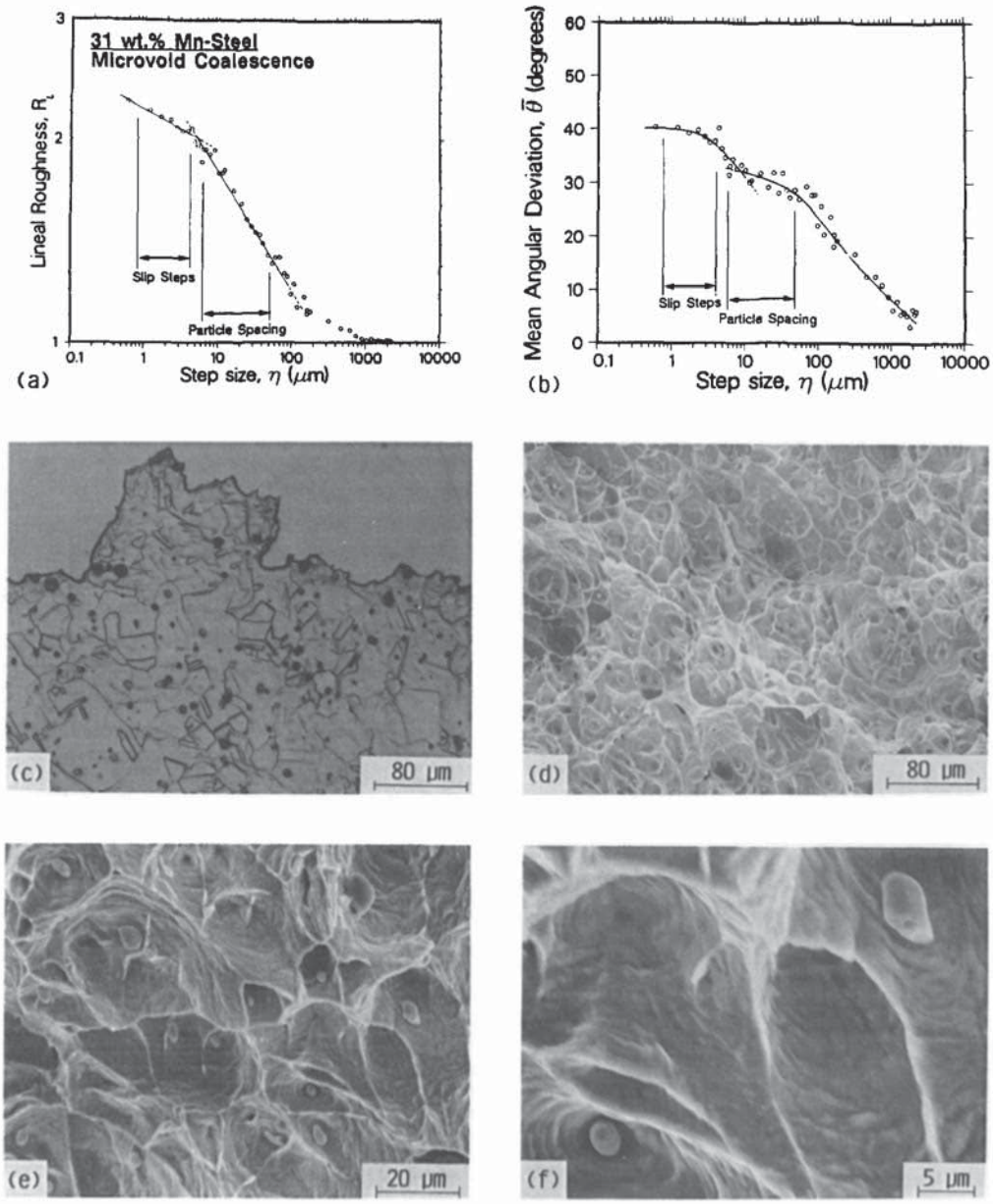

Fig. 10. Fractal characteristics of microvoid coalescence, of Mn-steel at room temperature, showing plots of (a) lineal roughness, R_L, and (b) mean angular deviation, $\bar{\theta}$, as a function of measuring step size, η, (c) optical micrograph of crack-surface profile, and (d–f) scanning electron micrographs of fracture surface at increasing magnifications.

be related to the mean and standard deviation of the segment distribution. A selected range of segment distributions was examined to discern the effects of mean segment length, mean angular deviation, standard deviation of the mean, and segment distributions of smaller mean lengths superimposed on the larger sized segment distributions to simulate both micro- and macro-roughness. Prediction of the value of the fractal dimension from parameters describing the segment distribution, however, awaits further analysis.

Where a second distribution of smaller segment lengths is superimposed on a larger one, two distinct ranges of fractal behavior, appropriate to the range of dimension of each distribution, are apparent. This may be understood as follows: on a scale less than the smallest segment size of the larger segment distribution, the curve becomes Euclidean; the linear roughness, R_L, parameter approaches a constant value independent of η. Roughness is then "added" to the otherwise flat Euclidean line by the superimposed smaller segment distribution and essentially begins a new fractal region ignorant of the fractal nature at larger scales.

The fractographic data obtained demonstrate that multiple values of the fractal dimension may occur

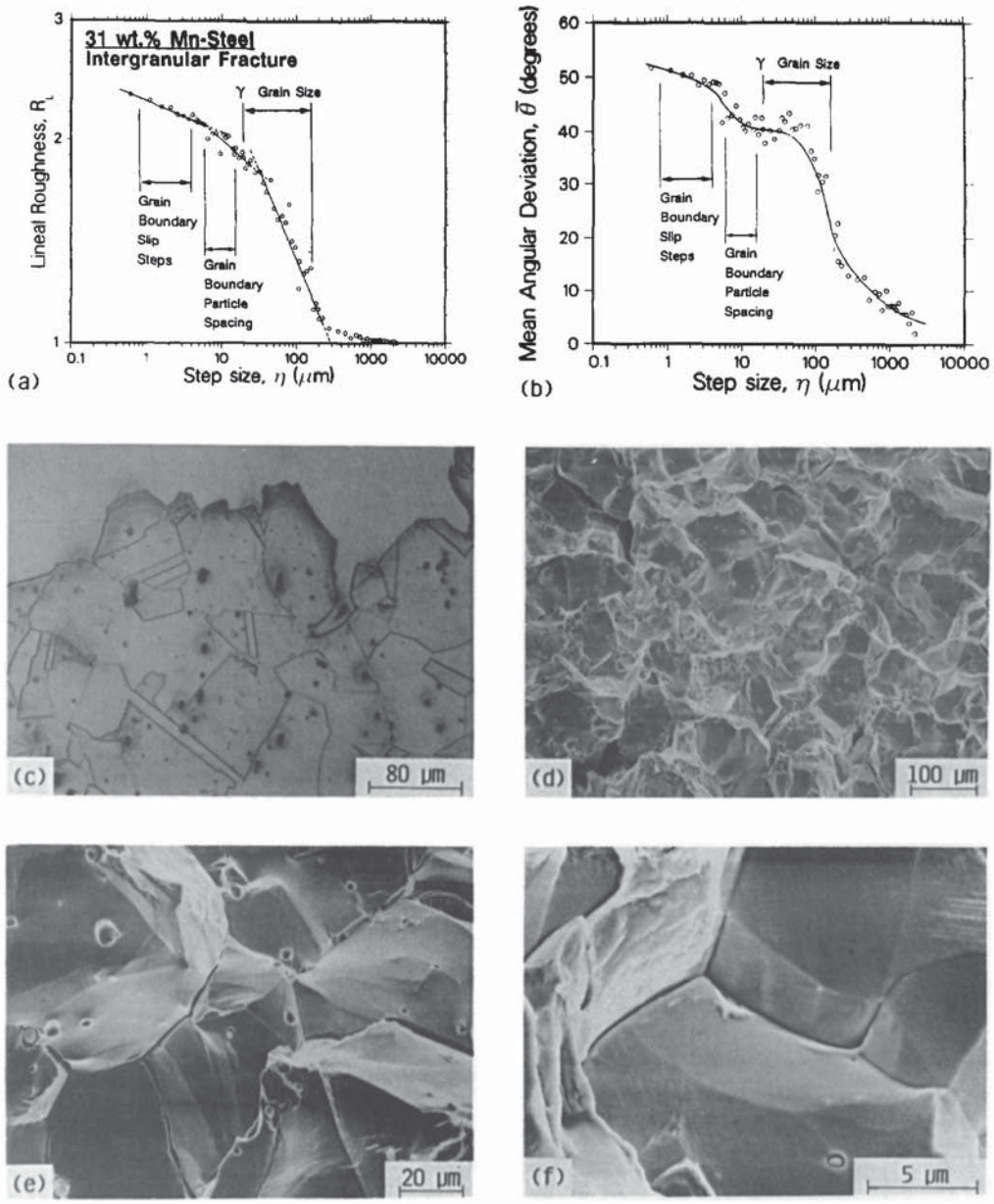

Fig. 11. Fractal characteristics of intergranular fracture, of Mn-steel at −196°C, showing plots of (a) lineal roughness, R_L, and (b) mean angular deviation, $\bar{\theta}$, as a function of measuring step size, η, (*c*) optical micrograph of crack-surface profile, and (d–f) scanning electron micrographs of fracture surface at increasing magnifications.

for a profile of a single fracture micromechanism, depending on the level of scrutiny. These discrete ranges of dimension, reflected by linear sections on the R_L/η plots, exhibit reasonable correlation with the size distribution of fractographic features evident on the fracture profile. For example, the transgranular cleavage fracture morphology (Fig. 9) exhibits two separate fractal regions corresponding to the dimensions of the cleavage step size and cleavage facet (and hence ferrite grain) size. Moreover, different fracture modes, such as microvoid coalescence and intergranular fracture, are clearly discernible in the same material by their different fractal dimensions, over size scales corresponding to the salient fractographic and microstructural features relevant to that mode (Figs 10 and 11).† Similar conclusions have been reached for the description of naturally-occurring seismological faults and fractures [36, 37].

†Results of the mean angular deviation $\bar{\theta}$ vs η did not display the same distinctive trends with level of observation observed for the R_L/η plots, although some correlation was apparent. $\bar{\theta}/\eta$ data have been included for completeness although are not considered as sensitive an indicator of characteristic fracture dimensions.

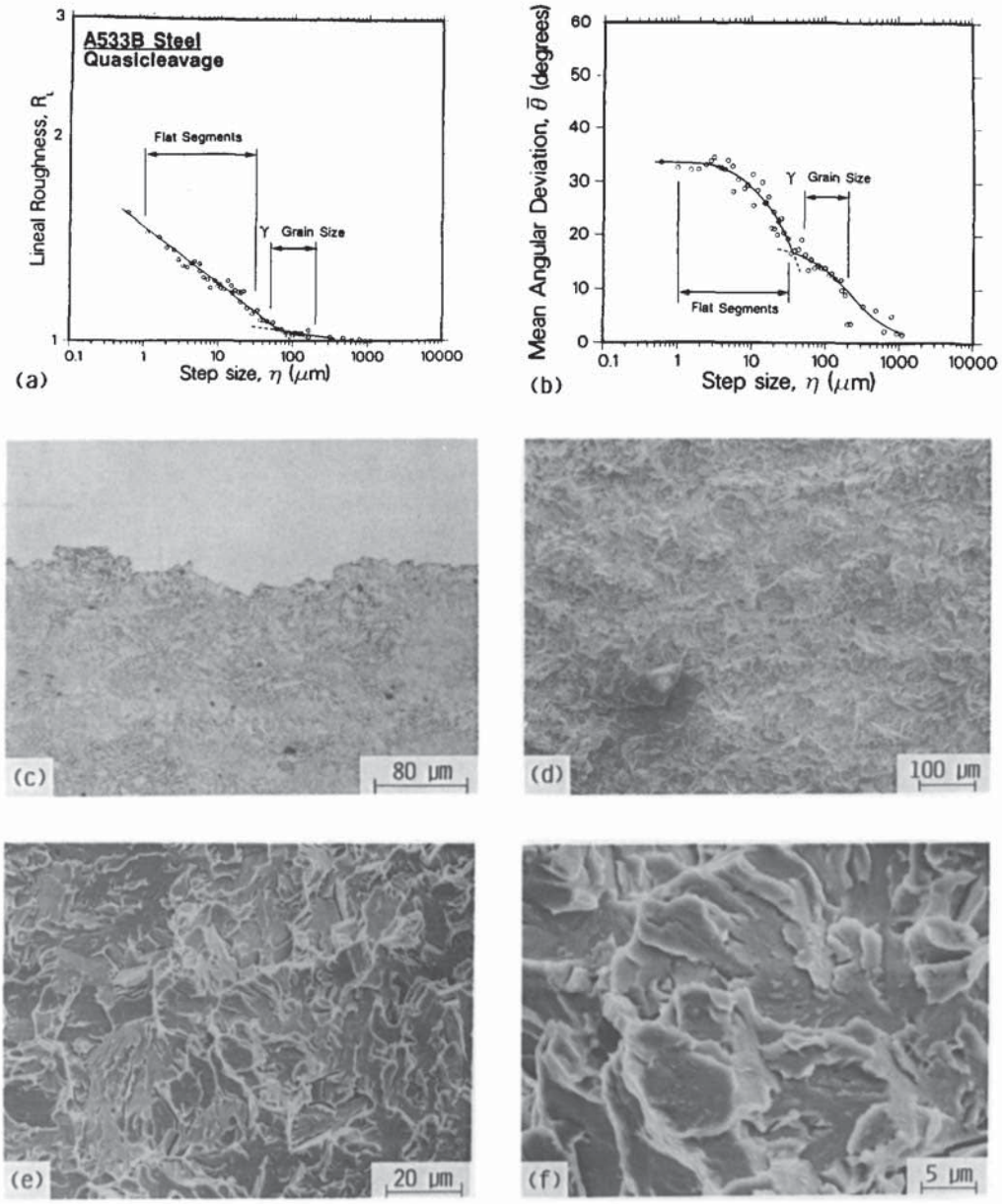

Fig. 12. Fractal characteristics of quasicleavage fracture, of A533B steel at −196°C, showing plots of (a) lineal roughness, R_L, and (b) mean angular deviation, $\bar{\theta}$, as a function of measuring step size, η, (c) optical micrograph of crack-surface profile, and (d–f) scanning electron micrographs of fracture surface at increasing magnifications.

The sensitivity of the fractal dimension as an indicator of subtle differences in fracture morphology, resulting for example from hydrogen-induced microstructural damage, is also clearly apparent (Figs 12–14). The increased R_L and D values of the fracture profile of hydrogen charged specimens reflect the effects of hydrogen embrittlement in increasing the roughness on the otherwise similar quasicleavage fracture surfaces of the charged and uncharged specimens (Figs 12 and 13). Furthermore, the fractal dimension provides information on the relative importance of microstructural features to the fracture process. In both hydrogen embrittled and hydrogen attacked conditions, the sensitivity of a particular microstructural feature to the damage mechanism is demonstrated by an increased fractal dimension in the size range of the appropriate feature; a higher D value over the dimensions of the prior austenite grain size in A533B steel is indicative of an increased contribution of this feature to the fracture morphology. More severe damage in the form of hydrogen attack is further apparent by an additional region of fractal behavior associated with the formation of microvoids on the grain-boundary surfaces at the smallest dimensions assessed (Fig. 14).

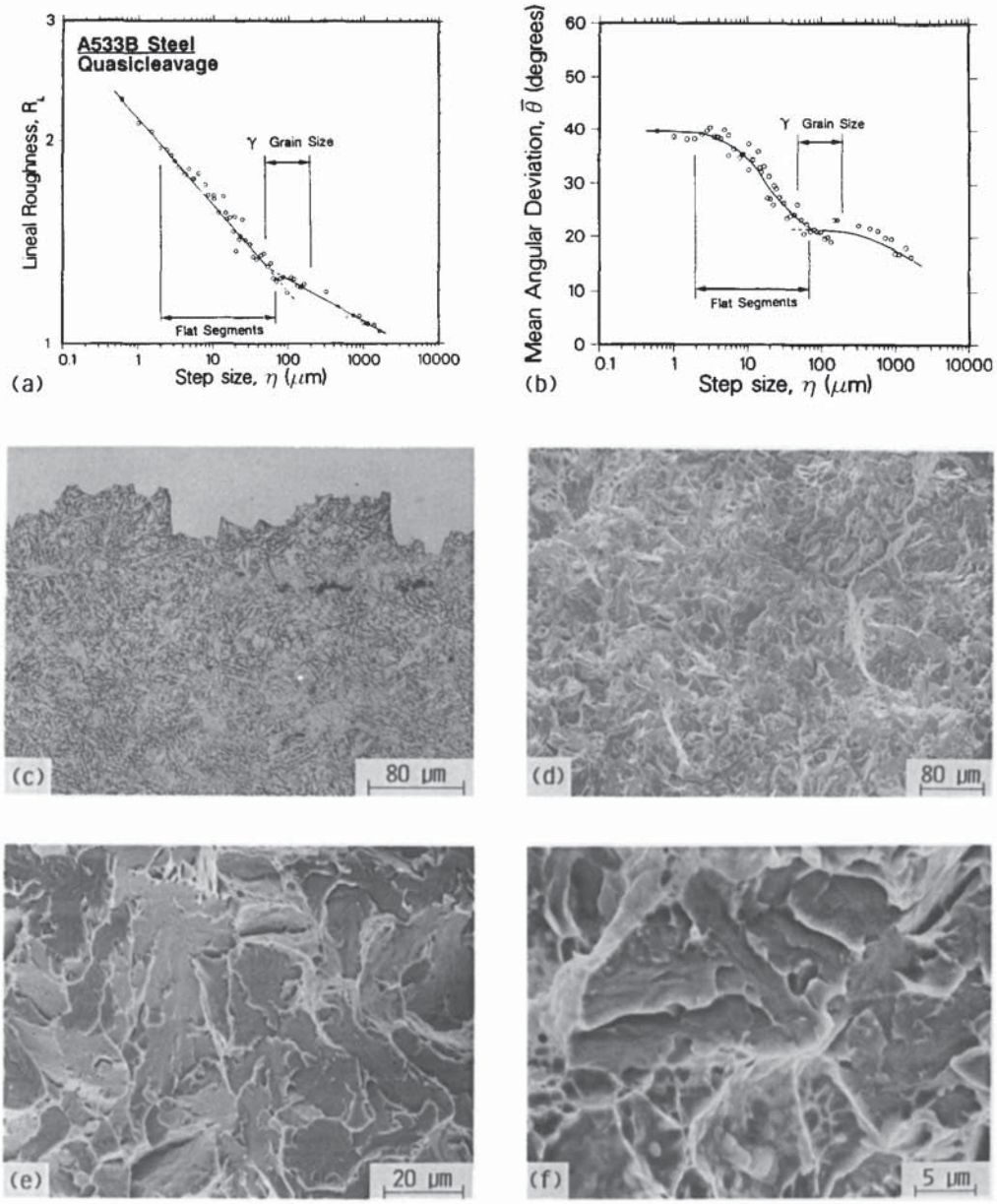

Fig. 13. Fractal characteristics of quasicleavage fracture, of hydrogen charged A533B steel at −196°C, showing plots of (a) lineal roughness, R_L, and (b) mean angular deviation, $\bar{\theta}$, as a function of measuring step size, η, (c) optical micrograph of crack-surface profile, and (d–f) scanning electron micrographs of fracture surface at increasing magnifications.

In light of the specificity of the fractal dimension to both the mode of fracture and level of scrutiny, universal relationships between the fractal dimension and fracture toughness or crack-growth resistance are clearly unlikely. However, where fracture-surface roughness is known to dictate the crack-growth behavior, specific correlations may be appropriate. Examples include ductile fracture, where the surface roughness associated with the microvoid shape can provide a measure of local fracture strain [21], brittle fracture in ceramic materials, where crack deflection involving tilts and twists of the crack path can result in a reduced local "crack driving force" and hence higher toughness [38], and near-threshold fatigue-crack growth [13], where the wedging action of enlarged fracture-surface asperities inside the crack (roughness-induced crack closure [30]) can exert a potent influence in impeding crack advance [13].

5. SUMMARY AND CONCLUSIONS

The present study investigates the applicability of fractal mathematics to the description of fracture-surface morphology. Specifically, this involved discerning the dimensions over which fractal behavior can exist, both theoretically in a series of numerically

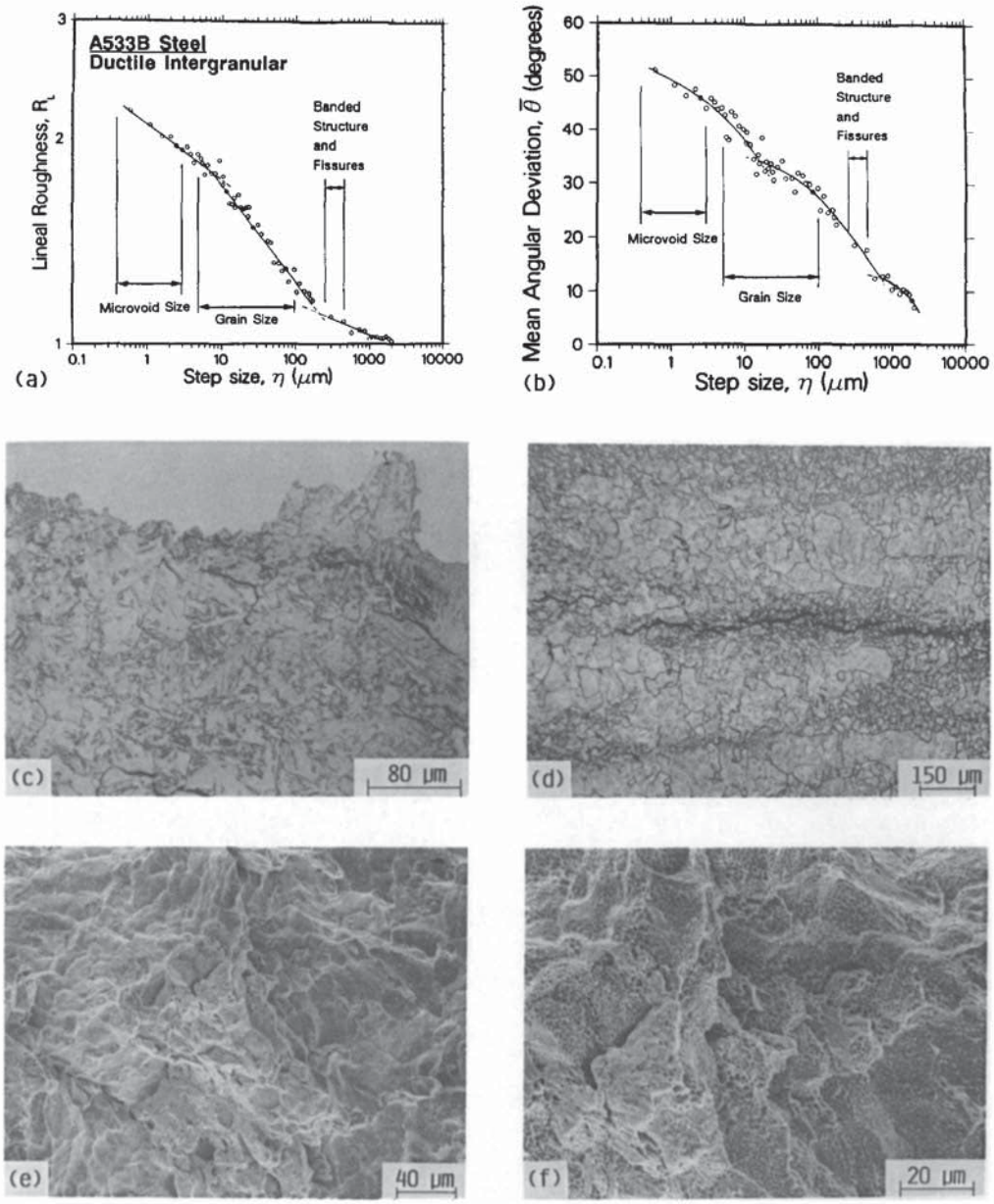

Fig. 14. Fractal characteristics of intergranular microvoid coalescence, of hydrogen attacked A533B steel at −196°C, showing plots of (a) lineal roughness, R_L, and (b) mean angular deviation, $\bar{\theta}$, as a function of measuring step size, η, optical micrographs of (c) crack-surface profile, and (d) fissure formation, and (e–f) scanning electron micrographs of fracture surface at increasing magnifications.

simulated fracture profiles, chosen systematically to vary such parameters as mean angular deviation and segment length, and experimentally in the major "classical" fracture mechanisms, where the salient microstructural and fractographic size-scales have been well characterized. Such results permit an enhanced interpretation of Richardson plots of lineal roughness R_L as a function of measuring step size η.

The following conclusions are made:

1. In simulated fracture-surface profiles, Gaussian distributions of segment lengths yield fractal character in R_L/η plots over well defined ranges of dimension which are included in the size range of that distribution; the extent of fractal character is related to the mean and standard deviation of the segment distribution used to create the profile.

2. Distinctive trends were observed for the mean angular deviation data with decreasing measuring step size and were exhibited over ranges of dimension in which fractal character is apparent for the simulated profiles, although similar correlations were not as pronounced for data from the fracture profiles. Mean angular deviation data are not considered as sensitive an indicator of characteristic fracture dimensions.

3. For the transgranular cleavage, brittle and ductile intergranular cracking, quasicleavage and

microvoid coalescence fracture mechanisms, fractal character is shown not to be singular for each mode; good correlation, however, is found between the extent of fractal behavior and several salient microstructural and fractographic features over a wide range of dimensions appropriate to the size distribution of those features.

4. In view of the specificity of fractal character to fracture mode, universal correlations between the fractal dimension and toughness are deemed unlikely. However, where fracture-surface roughness clearly affects crack-growth behavior, e.g. for microvoid coalescence, crack deflection in ceramics and during near-threshold fatigue, specific correlations may be appropriate.

Acknowledgements—This work was supported by the Director, Office of Energy Research, Office of Basic Energy Sciences, Materials Sciences Division of the U.S. Department of Energy under Contract No. DE-AC03-76SF00098. Thanks are due to Madeleine Penton for help in preparing the manuscript.

REFERENCES

1. B. B. Mandelbrot. *The Fractal Geometry of Nature*. Freeman, New York (1983).
2. H. E. Stanley and N. Ostrowsky, *On Growth and Form*, NATO ASI Series E, Appl. Sci., No. 100, Martinus Nijhoff. The Netherlands (1986).
3. P. Pfeifer, D. Avnir and D. Farin, *Surf. Sci.* **126,** 569 (1983).
4. P. Pfeifer and D Avnir, *J. chem. Phys.* **79,** 3558 (1983).
5. D. Avnir, D. Farin and P. Pfeifer, *J. chem. Phys.* **79,** 3566 (1983).
6. H. J. Stapleton, J. P. Allen, C. P. Flynn, D. G. Stinson and S. R. Kurtz, *Phys. Rev. Lett.* **45,** 1456 (1980).
7. A. J. Katz and A. H. Thompson, *Phys. Rev. Lett.* **54,** 1325 (1985).
8. B. H. Kaye, *Powder Technol.* **21,** 1 (1978).
9. B. H. Kaye, in *Particle Characterization in Technology*, pp. 81–100. CRC Press, Boca Raton, Fla (1978).
10. P. Longley and M. Batty, in *Measuring and Simulating the Structure and Form of Cartographic Lines*, Papers in Planning Research 102, Univ. of Wales, Inst. Sci. Technol., Cardiff, U.K. (1986).
11. B. B. Mandelbrot, D. E. Passoja and A. L. Paullay, *Nature, Lond.* **308,** 721 (1984).
12. K. Banerji and E. E. Underwood, "Fracture Profile Analysis of Heat Treated 4340 Steel," Technical Report, Fracture and Fatigue Research Laboratory, Georgia Institue fo Technology, Atlanta, GA (1986).
13. Z. G. Wang, D. L. Chen, X. X. Jiang, S. H. Ai and C. H. Shih, *Scripta metall.* **22,** 827 (1988).
14. C. S. Pande, L. E. Richards, N. Louat, B. D. Dempsey and A. J. Schoeble, *Acta metall.* **35,** 1633 (1987).
15. L. E. Richards and B. D. Dempsey, *Scripta metall.* **22,** 687 (1988).
16. E. Hornbogen, *J. Mater. Sci.* **21,** 3737 (1986).
17. A. R. Rosenfield, *Scripta metall.* **21,** 1359 (1987).
18. M. Coster and J. L. Chermant, *J. Mater. Sci.* **14,** 509 (1979).
19. E. E. Underwood and K. Banerji, *Mater. Sci. Engng* **80,** 1 (1986).
20. K. Banerji and E. E. Underwood, *Metall. Trans. A* **20A,** (1989). In press.
21. R. O. Ritchie and A. W. Thompson, *Metall. Trans. A* **16A,** 233 (1985).
22. R. O. Ritchie, J. F. Knott and J. R. Rice, *J. Mech. Phys. Solids* **21,** 395 (1973).
23. Tsann Lin, A. G. Evans and R. O. Ritchie, *J. Mech. Phys. Solids* **34,** 477 (1986).
24. R. O. Ritchie, L. C. E. Geniets and J. F. Knott, in *The Microstructure and Design of Alloys, Proc. ICSMA*-3, Vol. 1, pp. 124–128, Inst. of Metals & Iron and Steel Institute, London, U.K. (1973).
25. J. Kameda and C. J. McMahon, *Metall. Trans. A* **11A,** 91 (1980).
26. F. A. McClintock, *J. appl. Mech.* **35,** 363 (1968).
27. A. C. Mackenzie, J. W. Hancock and D. K. Brown, *Engng Fract. Mech.* **9,** 167 (1977).
28. R. O. Ritchie, W. L. Server and R. A. Wullaert, *Metall. Trans. A* **10A,** 1557 (1979).
29. R. E. Williford, *Scripta metall.* **22,** 197 (1988).
30. S. Suresh and R. O. Ritchie, in *Fatigue Crack Growth Threshold Concepts* (edited by D. L. Davidson and S. Suresh), pp. 227–261. Metall. Soc. AIME, Warrendale, Pa (1984).
31. M. L. Strum, *Ph.D. thesis*, Univ. of California, Berkeley, LBL Report No. LBL-22650, Lawrence Berkeley Laboratory (1986).
32. R. D. Pendse and R. O. Ritchie, *Metall. Trans. A* **16A,** 1491 (1985).
33. R. H. Dauskardt, R. D. Pendse and R. O. Ritchie, *Acta metall.* **35,** 2227 (1987).
34. Y. H. Kim and J. W. Morris, *Metall. Trans. A* **17A,** 1157 (1986).
35. T. Johannesson and A. Tholen, *J. Inst. Metals* **97,** 243 (1969).
36. C. H. Scholz and C. A. Aviles, in *Earthquake Source Mechanics* (edited by S. Das, J. Boatwright and C. Scholz), pp. 147–155. Am. Geophys. Univ., Washington, D.C. (1986).
37. C. H. Scholz, *Nature, Lond.* **336,** 761 (1988).
38. K. T. Faber and A. G. Evans, *Acta metall.* **31,** 565 (1983).